

# Comparison of Experimentally Measured and Computed Second-Mode Disturbances in Hypersonic Boundary-Layers

Christopher R. Alba\*

*Air Vehicles Directorate, Air Force Research Laboratory, Wright-Patterson AFB, OH 45433*

Katya M. Casper†

*School of Aeronautics and Astronautics, Purdue University, West Lafayette, IN 47907-1282*

*Sandia National Laboratories, Albuquerque, NM 87185*

Steven J. Beresh‡

*Sandia National Laboratories, Albuquerque, NM 87185*

Steven P. Schneider§

*School of Aeronautics and Astronautics, Purdue University, West Lafayette, IN 47907-1282*

Experiments were carried out in the Boeing/AFOSR Mach 6 Quiet Tunnel at Purdue University and the Sandia National Laboratories Hypersonic Wind Tunnel at Mach 5 and 8. The purpose was to measure second-mode boundary-layer instabilities on a  $7^\circ$  half-angle cone at zero angle of attack using surface pressure sensors. Second-mode waves were successfully measured at all three Mach numbers, including under both noisy and quiet conditions. The most amplified second-mode disturbance frequencies compared well to the linear Parabolized Stability Equations computed by the STABL software suite. The eigenfunctions are also reported, to aid in the development of new instrumentation methods. The  $e^N$  method is used in an attempt to determine the  $N$  factor for transition onset prediction in both tunnels.

## I. Introduction

Linear stability theory predicts that second-mode disturbances occur when there exists in the boundary-layer a region of supersonic flow relative to the disturbance phase velocity. Calculations and experiments have shown that second-mode disturbances are dominant, compared to lower frequency first-mode disturbances, when the edge Mach number is sufficiently high for a given wall temperature.<sup>1-4</sup> Second-mode disturbances are characterized as high frequency, acoustic wave type disturbances which were first identified by Mack.<sup>1</sup> This fact prompted the work of Stetson *et al.*<sup>2</sup> and Stetson and Kimmel<sup>3</sup> which used hot-wire anemometry to measure second-mode disturbances in a conventional wind tunnel. Additionally, measurements of second-mode waves have been carried out in the past with hot wires in both noisy and quiet flow.<sup>4</sup> Since these measurements are very difficult due to the limited mechanical strength of small hot wires with sufficiently high frequency response, an appropriate non-intrusive measurement technique is desirable.

---

\*1Lt, USAF, Member, AIAA

†Graduate Research Assistant and Student Intern, Student Member, AIAA

‡Principal Member of the Technical Staff, Engineering Sciences Center, Associate Fellow, AIAA

§Professor, Associate Fellow, AIAA

Report Documentation Page				Form Approved OMB No. 0704-0188	
Public reporting burden for the collection of information is estimated to average 1 hour per response, including the time for reviewing instructions, searching existing data sources, gathering and maintaining the data needed, and completing and reviewing the collection of information. Send comments regarding this burden estimate or any other aspect of this collection of information, including suggestions for reducing this burden, to Washington Headquarters Services, Directorate for Information Operations and Reports, 1215 Jefferson Davis Highway, Suite 1204, Arlington VA 22202-4302. Respondents should be aware that notwithstanding any other provision of law, no person shall be subject to a penalty for failing to comply with a collection of information if it does not display a currently valid OMB control number.					
1. REPORT DATE <b>JAN 2010</b>		2. REPORT TYPE		3. DATES COVERED <b>00-00-2010 to 00-00-2010</b>	
4. TITLE AND SUBTITLE <b>Comparison of Experimentally Measured and Computed Second-Mode Disturbances in Hypersonic Boundary-Layers</b>				5a. CONTRACT NUMBER	
				5b. GRANT NUMBER	
				5c. PROGRAM ELEMENT NUMBER	
6. AUTHOR(S)				5d. PROJECT NUMBER	
				5e. TASK NUMBER	
				5f. WORK UNIT NUMBER	
7. PERFORMING ORGANIZATION NAME(S) AND ADDRESS(ES) <b>Air Force Research Laboratory, Air Vehicles Directorate, Wright-Patterson AFB, OH, 45433</b>				8. PERFORMING ORGANIZATION REPORT NUMBER	
9. SPONSORING/MONITORING AGENCY NAME(S) AND ADDRESS(ES)				10. SPONSOR/MONITOR'S ACRONYM(S)	
				11. SPONSOR/MONITOR'S REPORT NUMBER(S)	
12. DISTRIBUTION/AVAILABILITY STATEMENT <b>Approved for public release; distribution unlimited</b>					
13. SUPPLEMENTARY NOTES					
14. ABSTRACT					
15. SUBJECT TERMS					
16. SECURITY CLASSIFICATION OF:			17. LIMITATION OF ABSTRACT <b>Same as Report (SAR)</b>	18. NUMBER OF PAGES <b>18</b>	19a. NAME OF RESPONSIBLE PERSON
a. REPORT <b>unclassified</b>	b. ABSTRACT <b>unclassified</b>	c. THIS PAGE <b>unclassified</b>			

Recently Fujii,<sup>5</sup> Estorf<sup>6</sup> and Tanno<sup>7</sup> have shown that fast surface PCB132 pressure transducers can measure the presence of second-mode disturbances on a cone in noisy hypersonic flow. This offers an advantage over hot-wire measurements because hot wires frequently break during the startup or shutdown of the tunnel. In the present work, this technique is used to measure the second mode under quiet and noisy flow conditions in the Boeing/AFOSR Mach-6 Quiet Tunnel (BAM6QT) of Purdue University and in the Sandia National Laboratories Hypersonic Wind Tunnel (HWT) at Mach 5 and 8. The measurements will be compared to linear Parabolized Stability Equations (PSE) computations using the STABL<sup>8</sup> suite.

## II. Experimental Setup

### II.A. Wind-Tunnel Facilities

#### II.A.1. Boeing/AFOSR Mach 6 Quiet Tunnel

The BAM6QT (Figure 1) can be operated as a conventional noisy tunnel or as a quiet tunnel. The BAM6QT is currently the only operational hypersonic quiet tunnel in the world. This makes it unique for boundary-layer transition studies. The tunnel is a Ludwig tube, a long tube with a converging-diverging nozzle on the end. The flow passes from the driver tube, through the test section, diffuser, a second throat, and finally to the vacuum tank. Flow is initiated by bursting a double diaphragm that is located downstream of the diffuser. When the flow begins, an expansion wave travels upstream and then reflects between the upstream end of the driver tube and the contraction. The total pressure and temperature drop with each reflection cycle (every 200 ms) until the tunnel unstarts. Run times of 3-5 seconds are typical at present. The tunnel uses air as the test gas and operates with an initial  $P_0$  of 34-2070 kPa and an initial  $T_0$  of 430 K, giving a  $Re/m$  range of  $0.4-18.3 \times 10^6$ . The current maximum quiet pressure ( $P_0$ ) is 1130 kPa which corresponds to  $Re/m = 10.5 \times 10^6$ . The test-section diameter is 0.241 m at the nozzle exit, and the nozzle is 2.590 m long. Noise levels (Pitot pressure fluctuations divided by the mean Pitot pressure) vary from 2-4.5% under noisy flow conditions.<sup>9</sup> Under quiet flow conditions, noise levels are approximately 0.05% or less.<sup>10</sup>

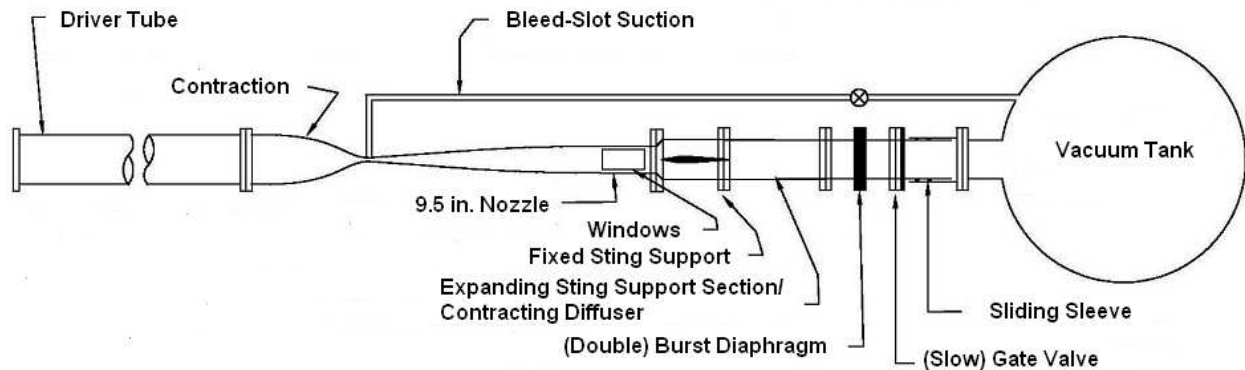


Figure 1. Schematic for Boeing/AFOSR Mach-6 Quiet Tunnel.

It is difficult to obtain quiet flow in a hypersonic tunnel. The nozzle is polished to a mirror finish to avoid roughness-induced transition. The contraction boundary-layer is also removed by bleed slots at the throat, for quiet runs. A new laminar boundary-layer begins just upstream of the nozzle throat and is maintained through the test section. The air is filtered to remove dust or other particles above 0.01 microns that may damage the nozzle or trip the boundary-layer. More details about the development of the BAM6QT can be found in Reference 11.

#### II.A.2. Sandia Hypersonic Wind Tunnel

The Sandia Hypersonic Wind Tunnel is a blowdown-to-vacuum facility (Figure 2). Interchangeable nozzle and heater sections allow the tunnel to be run at Mach 5, 8, or 14. Mach 5 tests use air as the driver gas while Mach 8 and Mach 14 run with nitrogen. Tests were only conducted at Mach 5 (HWT-5) and 8 (HWT-8) for this study because the Mach 14 heater was down for repairs. Run times were typically 15-30 seconds.

HWT-5 has a  $P_0$  range of 345-1380 kPa and a  $T_0$  range of 330-890 K, giving a  $Re/m$  range of  $3.3\text{-}26 \times 10^6$ . The test-section diameter is 0.459 m at the nozzle exit, and the nozzle is 3.251 m long, from the throat to the test-section end. Noise levels vary from 1-2% over the operating range of the tunnel.

HWT-8 uses 59 MPa nitrogen supplied from a bottle farm. It has a  $P_0$  range of 1720-6890 kPa,  $T_0$  range of 500-890 K, and  $Re/m$  can be varied from  $3.3\text{-}20 \times 10^6$ . The Mach 8 test-section diameter is 0.35 m at the nozzle exit, and the nozzle is 2.807 m long. Noise levels vary from 3-4.5% over the tunnel operating range.<sup>9</sup>

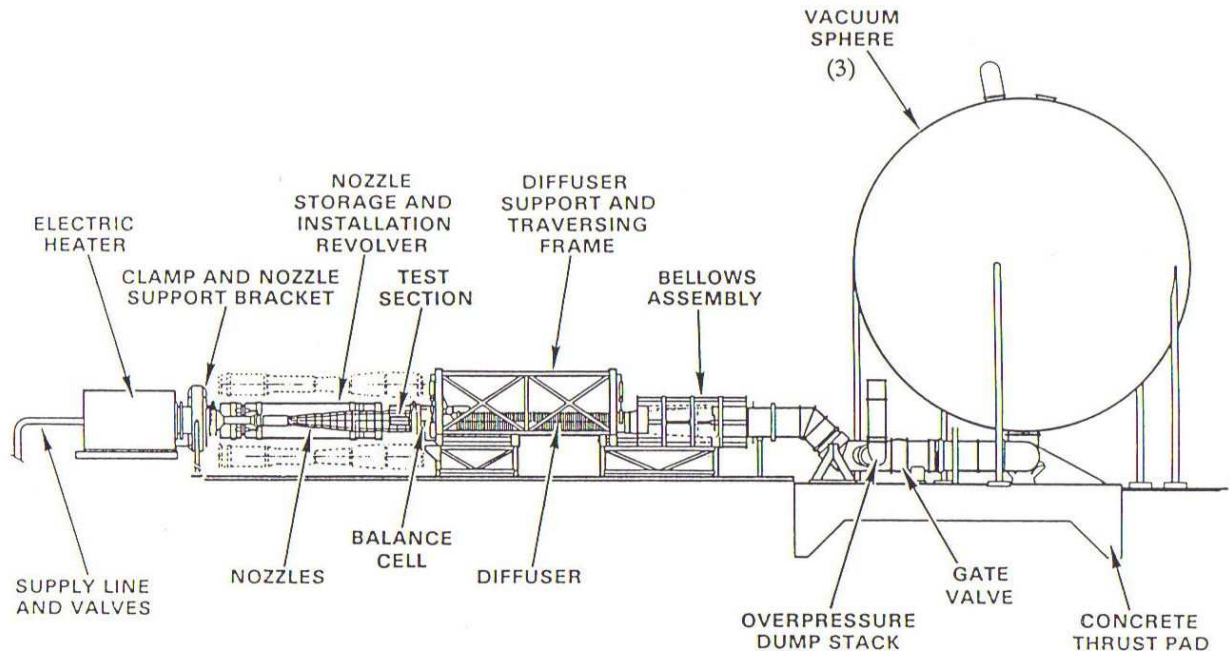


Figure 2. Schematic for Sandia Hypersonic Wind Tunnel.

## II.B. Model and Instrumentation

The Pressure-Fluctuation Cone was used for measurement of transitional pressure fluctuations. The model is a  $7^\circ$  half-angle stainless-steel cone, 0.517 m long. A sharp nose tip (radius less than 0.05 mm) was used for these tests. The instrumentation setup for testing had two rows for instrumentation spaced 120 degrees apart. Figure 3 shows the insert locations and Table 1 lists the location of these sensors, where  $x$  is the axial distance from the sharp nose tip and  $\phi$  is the cone azimuthal angle. More details about the Pressure-Fluctuation Cone, instrumentation and experiments are given in References 9 and 12.

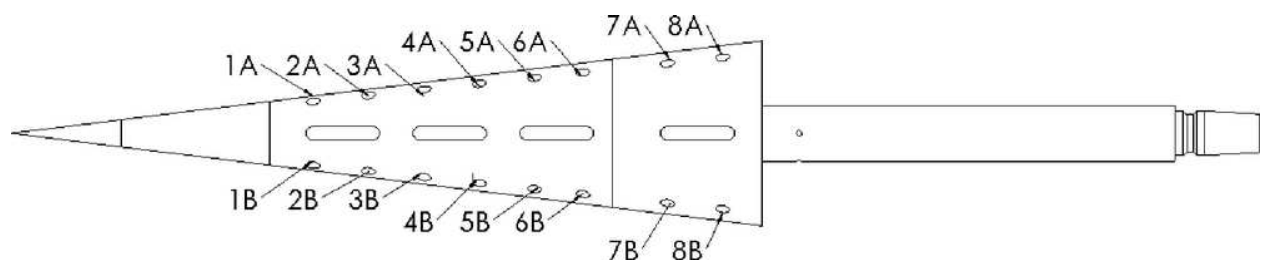


Figure 3. Individual sensor locations mounted on the  $7^\circ$  sharp cone.

The growth and breakdown of the second-mode wave instability leading to transition was studied with three PCB132 sensors at positions 1B, 5B, and 8B. The PCB132's were used to measure pressure fluctuations between 11 kHz and 1 MHz. The resonant frequency of the sensor is above 1 MHz; however, the sensor output is high-pass filtered with a 3-db cutoff frequency at 11 kHz, an inherent property of the sensor. Because of the high resonant frequency of the sensors, the PCB132's allow a study of instability breakdown to transition,

Location	$x$ (m)	$\phi$ (degrees)	Location	$x$ (m)	$\phi$ (degrees)
1A	0.208	0	1B	0.208	120
2A	0.246	0	2B	0.246	120
3A	0.284	0	3B	0.284	120
4A	0.322	0	4B	0.322	120
5A	0.360	0	5B	0.360	120
6A	0.398	0	6B	0.398	120
7A	0.452	0	7B	0.452	120
8A	0.490	0	8B	0.490	120

Table 1. Individual sensor axial and angular locations.

and are useful indicators of transition on the model. However, the sensors were designed as time-of-arrival sensors and have not yet been accurately calibrated for this purpose. In addition, the sensors have a sensitive area of  $1.6 \text{ mm}^2$ , which leads to spatial resolution problems for measuring such high-frequency instabilities. Second-mode waves have a wavelength of approximately twice the boundary-layer thickness (approximately 1-3 mm for this work). The PCB132 diameter (3.18 mm) is larger than half of the instability wavelength. Thus, some attenuation of the signal can be expected due to the limited spatial resolution of the sensor. The combination of an insufficiently calibrated sensor response and probable spatial attenuation may lead to bias errors in the amplitude of measured second-mode waves, though it is likely their frequency is correctly determined.

In order to compare the measured second-mode wave frequencies to computations, power spectral densities were calculated from the PCB132 data. The PCB132 time traces were first normalized by the boundary-layer edge pressure, taken from the Taylor-Maccoll solution for a sharp cone. The power spectral densities were then calculated for 0.1 second samples using Welch's method. A Blackman window with 25% overlap was used with a window size of 1024 points for HWT data and 2048 points for the BAM6QT. This gives a frequency resolution of 2.44 kHz. Approximately 976 FFT's were averaged. The resulting spectra can be compared to the maximum  $N$  factor versus frequency plots from stability computations. The ratio of spectra from different sensor locations can also be taken. The square root of this power spectral density ratio gives the amplitude ratio spectra between sensor locations, which can also be compared to computations.

## II.C. Data Acquisition

The data-acquisition systems at each facility are different but provide similar high-speed sampling and anti-aliasing over many channels.

### II.C.1. Boeing/AFOSR Mach-6 Quiet Tunnel

The PCB132 sensors all are powered by a PCB 482A22 signal conditioner that provides constant-current excitation to the built-in sensor amplifier. The constant current can be varied from 4 to 20 mA; 4 mA was used for all measurements. Two Tektronix DPO7054 and one Tektronix TDS7104 Digital Phosphor Oscilloscopes are used for data acquisition in the BAM6QT. The oscilloscopes have built-in digital filtering. Separate anti-aliasing filters are not required. The DPO7054 has a system bandwidth of 500 MHz and an 8-bit vertical resolution. The resolution can be increased to over 11-bit in Hi-Res mode. Hi-Res mode is used to increase the vertical resolution and reduce random noise. The oscilloscopes average real-time at the maximum sampling rate and then save data at the specified sampling rate. The TDS7104 has similar capabilities, but less memory. Five seconds of data were recorded for each run. The sampling rate was 5 MHz for the PCB132's.

### II.C.2. Sandia Hypersonic Wind Tunnel

As in BAM6QT, the PCB sensors connect to a PCB 482A22 signal conditioner. The output from the signal conditioner is fed through a Krohn-Hite Model 3944 Filter with a 1 MHz low-pass anti-aliasing Bessel filter. This filter has four poles and offers 24 dB of attenuation per octave. The sampling frequency for the PCB132

sensors was 2.5 MHz. Data are acquired using a National Instruments PXI-1042 chassis with 14-bit PXI-6133 modules (10 MHz bandwidth) for data acquisition. A data sample of 0.75 seconds was acquired during the constant-condition portion of each wind-tunnel run.

### III. Stability Computations

The laminar mean flows were solved as full Navier-Stokes solutions using an optimized 2D/axisymmetric solver based on the implicit Data-Parallel Line Relaxation (DPLR) method<sup>13</sup> which is provided with the stability code STABL.<sup>8</sup> The solver produces second-order accurate laminar flow solutions with low dissipation and shock capturing. For each of the simulations,  $300 \times 350$  point structured grids were generated with clustering both at the body surface and at the sharp nose tip. The wall temperature condition was isothermal at 303 K for all cases.

The flow for the BAM6QT and HWT-5 cases was considered to be a non-reacting mixture of 76.7% N<sub>2</sub> and 23.3% O<sub>2</sub> by mass. The flow for the HWT-8 cases was considered to be non-reacting pure N<sub>2</sub>. Freestream conditions were provided by the tunnel operators for each specific experiment. The specie viscosities were specified in a general fashion so that different viscosity models can be used through specified temperature ranges. Blending functions are used to maintain smooth function values and derivatives between models. Sutherland's viscosity law is used for temperatures up to 1550 K and then Blottner's viscosity model is used for temperatures higher than 1600 K. However, for these cases none of the temperatures were over 1550 K so Sutherland's law was only applied. The coefficients for air were used for the BAM6QT and HWT-5 cases while the coefficients for N<sub>2</sub> were used for the HWT-8 cases.

The linear PSE and LST analyses of the cases was performed using the PSE-Chem code which is distributed as a part of the STABL suite.<sup>8</sup> For the LST analysis, a parallel flow assumption was made by neglecting derivatives of mean flow quantities in the direction of the computational coordinate along the body. Spatial amplification rates and  $N$  factors of disturbances were found for given disturbance frequencies and surface locations. More details about the linear PSE approach used in STABL can be found in Reference 8. The computations were not performed differently for the noisy and quiet conditions of the BAM6QT, however, the interpretation of the stability results was different (i.e. use a different  $N$  for transition correlation).

## IV. Results

### IV.A. Second-Mode Frequency Comparisons

The freestream conditions for all cases considered are shown in Table 2. The freestream Reynolds number in Table 2 was calculated using Keye's Law for viscosity. Since we will be trying to compare with measured second-mode instabilities in the experiments, only two-dimensional (2D) waves have been considered for the stability calculations. The calculated most amplified second-mode disturbance frequencies are compared with the surface PCB132 pressure sensor measurements at  $x = 0.208$ ,  $0.360$  and  $0.490$  m. The results of those comparisons are shown in Figures 4-7. Some of the experimental results are missing from these figures because we do not currently have data at those specific axial locations, though they could be obtained in future runs. The results from STABL are obtained by first identifying all unstable frequencies at the specified axial location. Then the highest  $N$  factor achieved for each unstable frequency is recorded and the resulting curve is shown in the aforementioned figures. Overall, these figures illustrate that the computations and experiments agree well. Table 3 provides a more quantitative analysis of the second-mode frequency comparison. The following analysis will only be comparing most amplified frequencies, and there is only a limited attempt to compare amplitudes due to uncertainties regarding such measurements from the PCB132 sensors.

Figure 4 has comparisons for Cases 1-3 in the BAM6QT at Mach 5.8, which highlights the effect of an increasing unit Reynolds number. At the lowest unit Reynolds number, the signal-to-noise ratio is low and clear frequency peaks are difficult to determine from the experimental measurements. At a unit Reynolds number of  $6.4 \times 10^6 \text{ m}^{-1}$ , the computed and measured most unstable disturbance frequencies differ by less than 4% at both  $x = 0.208$  m and  $x = 0.360$  m. The flow has become turbulent at  $x = 0.490$  m. Higher harmonics start to become significant at  $x = 0.360$  m since a second peak can be observed in the measurement. Nonlinear effects will become a critical part of the second-mode transition process after this



Case	Tunnel	Flow	$M_\infty$	$P_o$ (kPa)	$T_o$ (K)	$Re/m \times 10^6$	Test Gas
1	BAM6QT	Noisy	5.8	274	429	2.9	Air
2	BAM6QT	Noisy	5.8	602	429	6.4	Air
3	BAM6QT	Noisy	5.8	795	429	8.5	Air
4	BAM6QT	Noisy	5.8	937	416	10.4	Air
5	BAM6QT	Quiet	6.0	1043	427	10.3	Air
6	HWT-5	Noisy	4.93	432	483	5.7	Air
7	HWT-5	Noisy	4.93	607	442	9.1	Air
8	HWT-8	Noisy	7.82	2414	759	5.0	$N_2$
9	HWT-8	Noisy	7.87	3296	606	9.5	$N_2$

**Table 2. Run conditions for BAM6QT and Sandia HWT second-mode wave measurements.**

axial location. The highest unit Reynolds number case in Figure 4 again shows great agreement at the first measurement location, but it is difficult to determine the frequency peak at  $x = 0.360$  m since the transition process has started and the flow is clearly turbulent by the end of the cone. The experimental results at  $x = 0.360$  m could also be showing nonlinear wave growth.

Cases 4 and 5 illustrate the difference between noisy and quiet wind tunnel measurements at similar freestream unit Reynolds numbers, as shown in Figure 5. There are two major differences to point out between these plots. The first is that Case 4 transitioned by  $x = 0.360$  m and Case 5 remained laminar. The second is the huge difference in wave amplitude between the noisy and quiet experimental measurements. We are able to almost match exactly the second-mode frequency peak at  $x = 0.208$  m for Case 4. The wave growth in Case 5 is not able to overcome electrical noise at the same axial location or the wave is not present, but either way the second-mode wave is not evident. A frequency peak can finally be detected at  $x = 0.490$  m for Case 5, which still matches the computational result to within 5%.

The worst comparison between computations and experiments came from Cases 6 and 7, which were conducted in HWT-5 and are shown in Figure 6. The experimental measurements at the first sensor location did not show evidence of second-mode waves and is omitted for clarity due to large noise spikes. For both cases, identifying a definitive frequency peak becomes nearly impossible from the experimental measurements. We are able to approximate an experimental frequency peak for Case 6 at  $x = 0.490$  m and for Case 7 at  $x = 0.360$  m, for which we get a 14% error in comparison to the computational result for both cases. The flow becomes turbulent by  $x = 0.490$  m for Case 7 and a  $N$  factor comparison will be made in a later section of this paper. It is unknown as to why the computations and experiments do not agree for these HWT-5 cases but we suspect discrepancies due to second-mode waves not being the dominant transition mechanism and possible nonlinear wave growth effects. A first-mode disturbance analysis will be performed in a later section to further investigate the causes of transition.

The last set of comparisons are shown in Figure 7 for Cases 8 and 9. These wind tunnel tests were conducted in HWT-8 with an increase in unit Reynolds number from Case 8 to 9. Case 8 provides an excellent picture of almost the entire transition process. At the first measurement location, the computed second-mode frequency peak is within 5% of the measured peak and since higher harmonics are not present, we believe that this is still the linear growth stage. A second higher harmonic can be seen in the normalized pressure fluctuation at  $x = 0.360$  m, but the computations still accurately predict the most amplified second-mode frequency to within 4%. By  $x = 0.490$  m, transition onset has been observed in the experiment but the flow is not fully turbulent yet. From the experimental measurement, the peak second-mode frequency is becoming diminished by the other higher harmonics present in the signal and we are seeing a more broadband frequency spectrum. However, the computed and measured second-mode peak frequency still compare well with a 5% difference. Case 9 has a transition onset location before  $x = 0.360$  m so, meaningfully, we are only able to compare the first measurement location with the computation. The computed and measured peak second-mode frequency were within 2% of each other at  $x = 0.208$  m.

One of the best methods for comparing to the experimental data is to integrate the computed amplification rates and compare the amplitude ratio to the experimental value.<sup>14</sup> This comparison was attempted with the experimental measurements, however many problems were encountered. In conventional hypersonic wind tunnels, there is a finite amount of freestream tunnel noise, typically above electronic noise levels. In order

to detect the second-mode waves, the waves must grow above that tunnel noise. This limits the smallest detectable size of the waves. In the present experiments under noisy flow, when the waves were large enough to be detected at an upstream sensor location, they were always nonlinear by the subsequent sensor. These nonlinearities prevented an effective comparison to the linear computations. Closer sensor spacing is needed to obtain linear measurements at two sensor locations under noisy flow conditions.

Under quiet flow conditions, the freestream tunnel noise is no longer the limiting threshold for instability detection. Instead, the limiting factor is the electrical noise, which is still present in the measurements. In the current quiet-flow experiments, the sensor spacing was again too large to allow an effective comparison of wave growth. Upstream sensor locations measured only electrical noise, while second-mode waves were only measured at the last sensor location on the cone. A repeat of these experiments with closer sensor spacing should allow a better comparison to computations. However, these comparisons will always be difficult because of the electrical and freestream tunnel noise in the experiments. Controlled perturbations may be necessary to enable good comparisons. The uncertainty in the PCB132 amplitude measurements will also need to be better quantified to improve these comparisons.

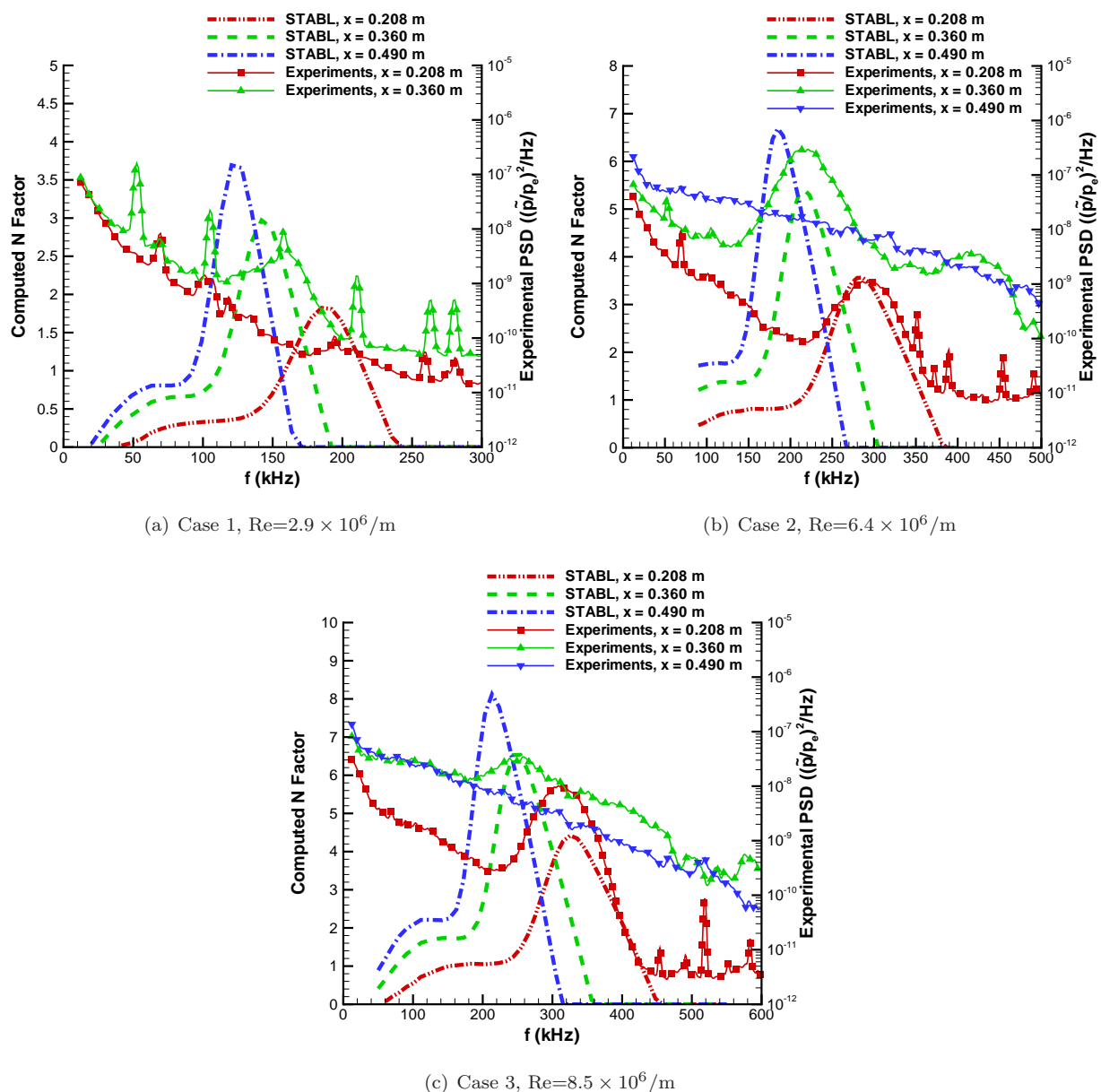


Figure 4. Comparison of most amplified second-mode disturbance frequency for Cases 1-3. These experiments were run noisy at Mach 5.8 in the BAM6QT and with air as the test gas.



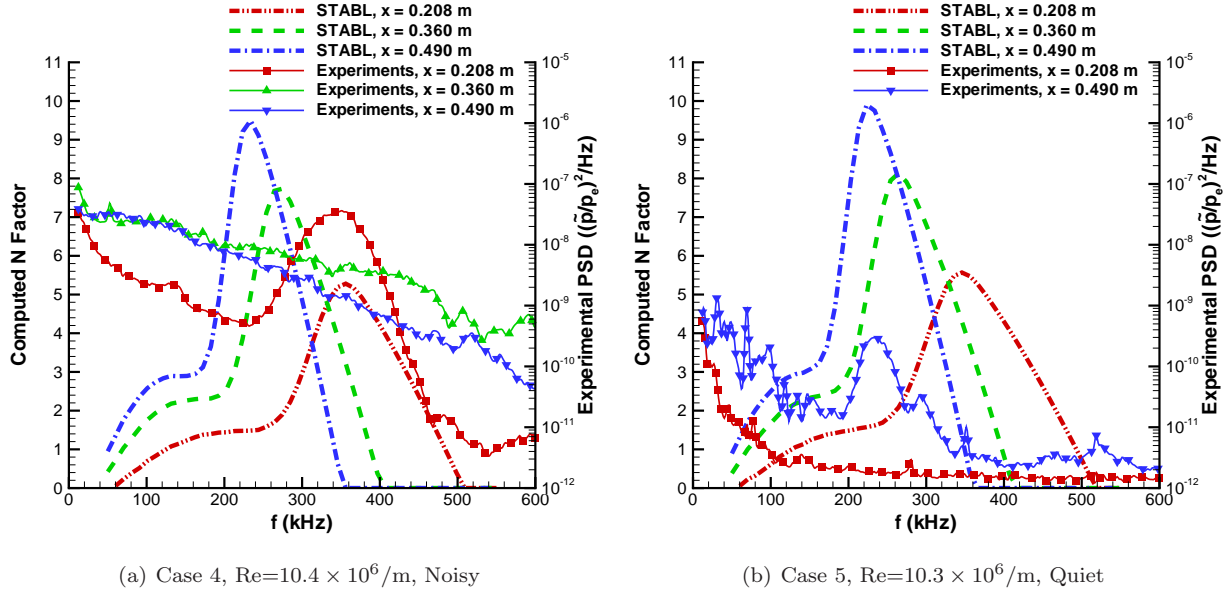


Figure 5. Comparison of most amplified second-mode disturbance frequency for Cases 4 and 5. Case 4 was run noisy at Mach 5.8 and Case 5 was run quiet at Mach 6.0. Both cases were in the BAM6QT and with air as the test gas.

#### IV.B. Eigenfunction Analysis

Instability waves that lead to transition are generally small disturbances traveling at high speed. These lead to high frequencies that are difficult to measure.<sup>15</sup> Instabilities can also take the form of stationary waves that grow as they move downstream. The design of the measurement apparatus should take advantage of what is known about the particular kinds of instability waves that are of interest. Waves have been measured with hot wires, surface hot films, surface thin films, surface pressure sensors, the laser differential interferometer, and other devices. Each instrument has advantages and disadvantages in particular cases.

The linear analysis of wave amplification readily generates the frequencies of the amplified waves, and their amplification rates. The amplification rates can be integrated for comparison to experimental measurements at various streamwise stations.

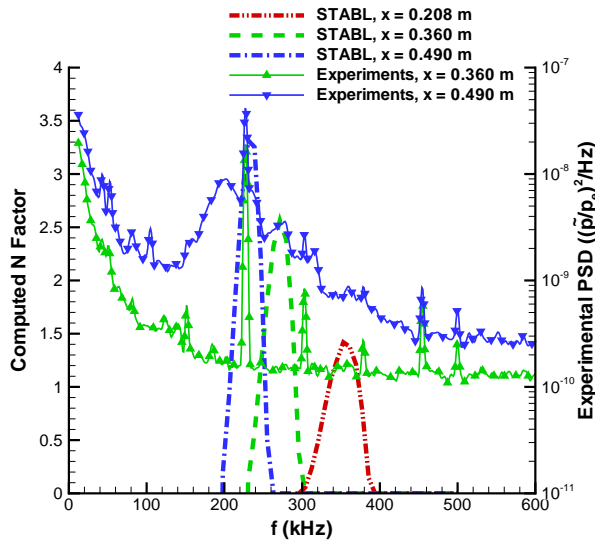
The linear analysis also generates the spatial distribution of the wave properties, generally in the form of eigenfunctions. This is also critical information for design. Although the wave amplifies as it goes downstream, and the usual linear analyses cannot specify the amplitude, the relative amplitudes of the various wave components generally remain fairly consistent. The wave amplitude can be normalized in some fashion, using edge or wall conditions that are fairly readily controlled. The eigenfunction plots then show what aspects of the wave are more readily measured.

A more detailed analysis of the disturbance eigenfunctions obtained from the simulations will be presented next for Case 2. The disturbance eigenfunctions are obtained from the solution of the parabolized disturbance equations, which is shown as Eq. 13 in Reference 8. The disturbance vector,  $\phi$ , is defined as:

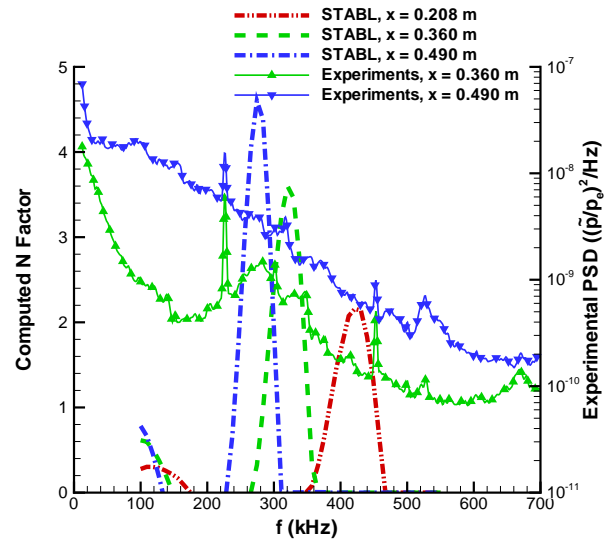
$$\phi = \psi(x, y) e^{i(\int \alpha dx + \beta z - \omega t)}$$

where  $\psi$  is the shape function or disturbance eigenfunction, which is complex so it has amplitude and phase,  $\alpha$  is the complex streamwise wavenumber which contains the disturbance amplification rate ( $-\alpha_i$ ),  $\beta$  is the spanwise disturbance wavenumber and  $\omega$  is the disturbance frequency. From the shape function, we get disturbances in all of the flow variables. In general, the primitive variables are  $\rho_s$ ,  $u$ ,  $v$ ,  $w$ ,  $T$  and  $T_v$ . For the pressure and heat transfer, the fluctuation is a combination of fluctuations of the primitive variables along with mean flow quantities. For example, we can compute the pressure fluctuation, which is a complex function, and take the magnitude of this complex function. This is what we call the amplitude of the pressure fluctuation. Now, since we are solving a linear problem, we can arbitrarily scale the fluctuation amplitude to some value.

The LST stability diagram for Case 2 is shown in Figure 8, which will provide the most unstable disturbance frequencies at each PCB sensor location. We will focus on the  $x = 0.208$  m sensor location for most of

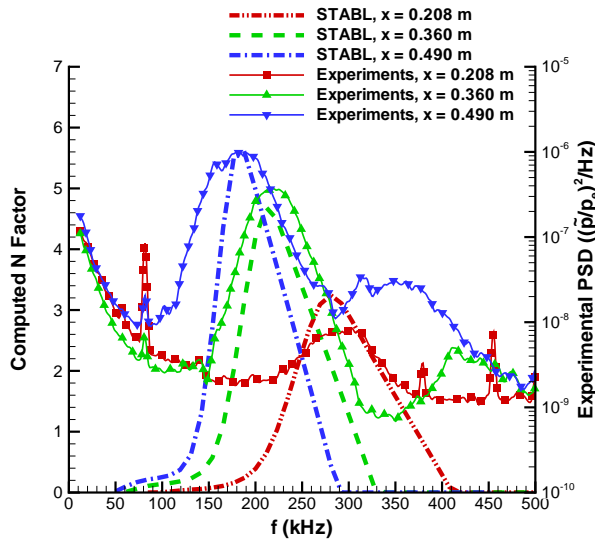


(a) Case 6,  $Re=5.7 \times 10^6/m$

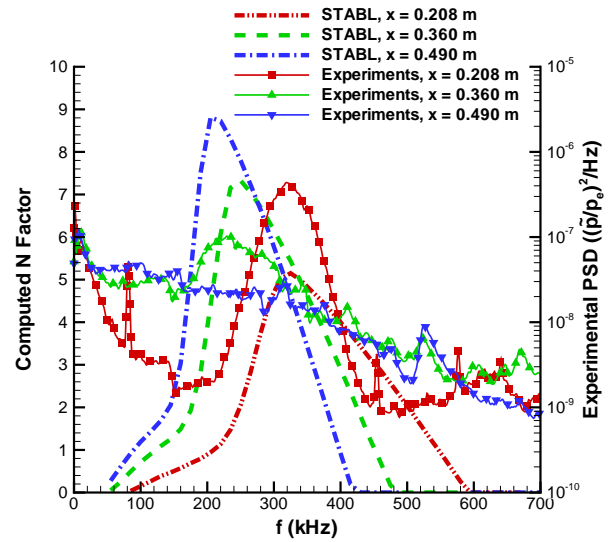


(b) Case 7,  $Re=9.1 \times 10^6/m$

Figure 6. Comparison of most amplified second-mode disturbance frequency for Cases 6 and 7. These experiments were run noisy at Mach 4.93 in the HWT-5 and with air as the test gas.



(a) Case 8,  $Re=5.0 \times 10^6/m$



(b) Case 9,  $Re=9.5 \times 10^6/m$

Figure 7. Comparison of most amplified second-mode disturbance frequency for Cases 8 and 9. These experiments were run noisy at approximately Mach 7.8 in the HWT-8 and with  $N_2$  as the test gas.

Case	Tunnel	$Re/m \times 10^6$	$x$ (m)	STABL Peak (kHz)	Experiment Peak (kHz)
1	BAM6QT	2.9	0.208	186	195
1	BAM6QT	2.9	0.360	142	160
1	BAM6QT	2.9	0.490	121	No Data
2	BAM6QT	6.4	0.208	286	297
2	BAM6QT	6.4	0.360	216	221
2	BAM6QT	6.4	0.490	186	Turbulent
3	BAM6QT	8.5	0.208	325	318
3	BAM6QT	8.5	0.360	254	258
3	BAM6QT	8.5	0.490	214	Turbulent
4	BAM6QT	10.4	0.208	356	350
4	BAM6QT	10.4	0.360	275	Turbulent
4	BAM6QT	10.4	0.490	234	Turbulent
5	BAM6QT	10.3	0.208	345	Noise
5	BAM6QT	10.3	0.360	265	No Data
5	BAM6QT	10.3	0.490	224	236
6	HWT-5	5.7	0.208	353	Noise
6	HWT-5	5.7	0.360	273	Noise
6	HWT-5	5.7	0.490	230	202
7	HWT-5	9.1	0.208	422	Noise
7	HWT-5	9.1	0.360	320	282
7	HWT-5	9.1	0.490	275	Turbulent
8	HWT-8	5.0	0.208	281	298
8	HWT-8	5.0	0.360	212	220
8	HWT-8	5.0	0.490	188	179
9	HWT-8	9.5	0.208	324	319
9	HWT-8	9.5	0.360	250	229
9	HWT-8	9.5	0.490	205	Turbulent

Table 3. Calculated and measured most unstable second-mode disturbance frequencies at the surface pressure sensor locations.

this analysis. Second-mode disturbances are unstable in the 220-295 kHz range at  $x = 0.208$  m. Figure 4b shows that the largest  $N$  factors were generated at about 286 kHz.

In this analysis, the overall amplitude of the disturbances is set by first scaling all of the components of the disturbances by the factor which results in a maximum amplitude of pressure fluctuation of 1% of the freestream pressure at  $x = 0.208$  m. Figure 9 shows the resulting instantaneous pressure that would be measured on the wall for a 286.44 kHz disturbance, along with the laminar steady pressure. Figure 10 shows the peak amplitudes of the wall pressure and heat flux fluctuations, normalized by the wall values of the mean flow quantities. The three frequencies shown were the most unstable at each respective pressure sensor location. Hence, 286.44 kHz was the most unstable at  $x = 0.208$  m, 214.44 kHz at  $x = 0.360$  m and 184.44 kHz at  $x = 0.490$  m. These frequencies also matched the second-mode peak frequencies in the experimental results, as seen in Figure 4b, except at  $x = 0.490$  m because the flow had become turbulent. It is important to note that the heat flux fluctuation amplitudes normalized by the mean wall values are larger than the pressure fluctuation amplitudes normalized by the mean wall values. It may be easier to experimentally measure heat flux fluctuations, although this will also depend on specific sensor characteristics. Figure 11 shows the disturbance eigenfunctions as a function of the normalized distance from the wall. Each disturbance amplitude component is normalized by its respective wall or edge mean flow value.

We see the peak value of 286.44 kHz at 0.005 in Figure 11a because the pressure fluctuation amplitude is normalized by the wall pressure. Following the exact calculation, the initial pressure fluctuation amplitude

is scaled to 1% of the freestream pressure. The freestream pressure is approximately 470 Pa and 1% of this is 4.7. If the pressure fluctuation amplitude is plotted after this scaling, the peak value of 286.44 kHz is 4.6. This peak is about 1% of the freestream pressure, and there may be another frequency near 286.44 kHz that will give the exact 4.7 value. The wall pressure is approximately 912 Pa. Performing the normalization,  $4.6/912$  equals 0.005, which is exactly what Figure 11a is showing for 286.44 kHz.

Mass flow fluctuations in second-mode waves can be measured with a hot wire, but these are small except near the edge of the boundary layer. The current results have highlighted the substantial pressure fluctuations associated with second-mode waves, which can be measured with wall sensors, if the wall sensors are sufficiently small relative to the wavelength. An improved understanding of the spatial variations in the waves and of the relative amplitudes of the various components of the fluctuations will aid in the design of future instrumentation.

#### IV.C. Estimated Transition Location Comparison

The computed maximum  $N$  factors for all cases is shown in Figure 12. Johnson *et al.*<sup>16</sup> and Alba *et al.*<sup>17</sup> suggest that a  $N$  factor value of 5.5 provides a good, rough estimate for predicted transition locations in conventional wind tunnels. The value of  $N$  at transition for smooth-body geometries in low disturbance freestream conditions, such as quiet wind tunnels or free-flight, has been shown to be about 8-11.<sup>18-21</sup> Using these criteria, Table 4 compares the estimated and observed transition onset locations. Obviously, for Case 5 we would not use the  $N = 5.5$  criterion since the tunnel was run quiet. Normally a  $N$  factor of 10 is used to attempt a correlation in low disturbance environments, however the computed  $N$  factor reached exactly 10 at the end of the cone without the flow transitioning in the experiment.

The experimental transition onset location is defined using the point of peak pressure fluctuations determined by lower-frequency (0 to 50 kHz) pressure measurements at positions 1 through 8 (Figure 3). The sensor spacing between these positions varies between 0.38 and 0.53 m, limiting the resolution in determining transition onset. The lower bound and upper bounds of the estimated transition onset location are shown in Table 4. These lower-frequency measurements as well as the determination of transition onset location are discussed in References 9 and 12.

The four BAM6QT cases that were run noisy all had  $N$  factors at the experimental estimated transition onset location lower than 5.5. Case 1 did not transition in the experiment but also only achieved a maximum  $N$  factor of 3.7 by the end of the cone. A  $N$  factor range that correlates transition better with the experiment would be between 4.5-5.0. This  $N$  factor range would also still be in agreement with Case 1 for predicting laminar flow. The lower  $N$  factor correlation for conventional noise transition in BAM6QT is not surprising. Comparing to the  $N = 5.5$  correlation in Reference 17, the BAM6QT is smaller so the noise level is higher than at Calspan University at Buffalo Research Center or NASA Langley Research Center. The two HWT-8 cases had correlating  $N$  factors at the experimental estimated transition onset location above and slightly below 5.5. Hence, this criterion may be applicable but more tests are needed to build the database for this tunnel until a more definitive correlation can be determined.

The computed maximum  $N$  factors for the two HWT-5 cases did not achieve 5.5, however transition onset was detected before the end of the cone in both cases. The experimental transition onset locations had  $N$  factor ranges between 3.1-3.3 for Case 6 and 3.6-3.7 for Case 7. The edge Mach numbers for these cases was below five as seen in Figure 13, which could indicate that second-mode disturbances may not be the most dominant disturbance. The boundary-layer edge is defined as the distance above the wall where 99.5% of the total enthalpy has reached its freestream value. Also, the HWT-8 cases have larger tunnel noise than the HWT-5 cases, yet transition occurred at a lower  $N$  factor for the HWT-5 cases. This may be more evidence that transition is not second-mode dominant.

Since it appears we do not have significant second-mode growth to instigate transition, a first-mode oblique wave disturbance analysis was performed for Case 6. The results of the first-mode analysis are combined with the second-mode results in Figure 14. Figures 14a-c displays the 3D stability diagram for the first-mode oblique wave instabilities along with the 2D stability diagram of the second-mode acoustic wave instabilities at the  $\beta = 0$  plane. The 2D stability diagram at the  $\beta = 0$  plane displays the amplification rate contours labeled as  $-\alpha_i$  (1/m). The first-mode oblique wave disturbance amplification is represented by an isosurface at an amplification rate level of  $1 \text{ m}^{-1}$ . First-mode disturbances will be unstable within this isosurface. Finally, this isosurface level is colored by the corresponding wave angle  $\psi$ , which is related to the spanwise wavenumber  $\beta$ . See Reference 22 for more details concerning the  $\psi - \beta$  relations. From these first-mode stability results, the peak amplification rate at each axial location and disturbance frequency,

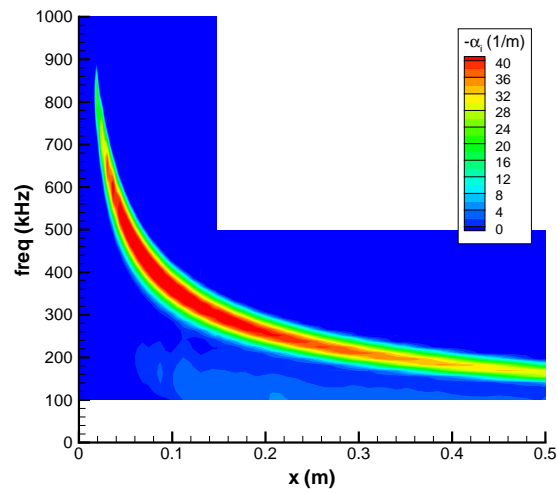
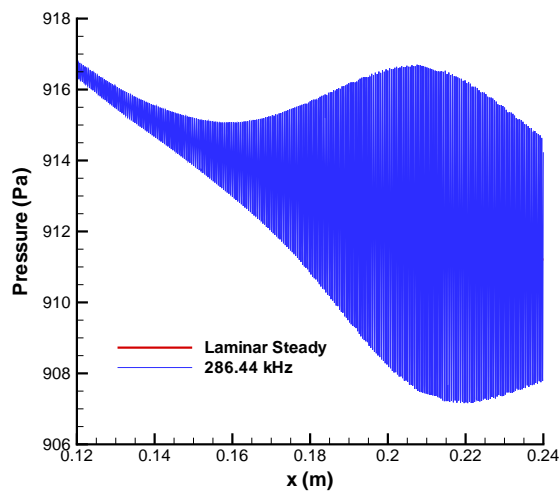
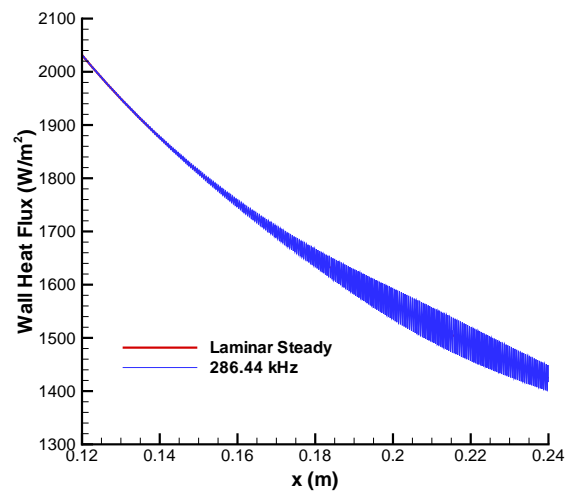


Figure 8. LST stability diagram for Case 2.

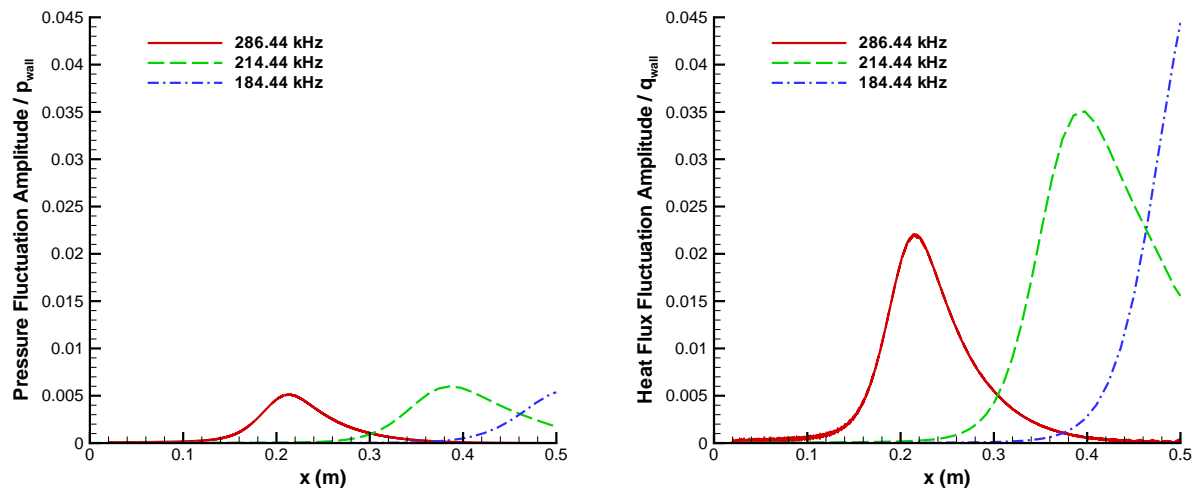


(a) Pressure fluctuations



(b) Wall heat flux fluctuations

Figure 9. Case 2 instantaneous wall pressure and wall heat flux fluctuations for a 286.44 kHz disturbance scaled to maximum pressure fluctuations of 1% of freestream pressure.



(a) Wall pressure fluctuation amplitudes normalized by wall pressure (b) Wall heat flux fluctuation amplitudes normalized by wall heat flux

Figure 10. Peak amplitudes of wall pressure and wall heat flux fluctuations scaled to maximum pressure fluctuations of 1% of freestream pressure and normalized by wall pressure and wall heat flux for Case 2.

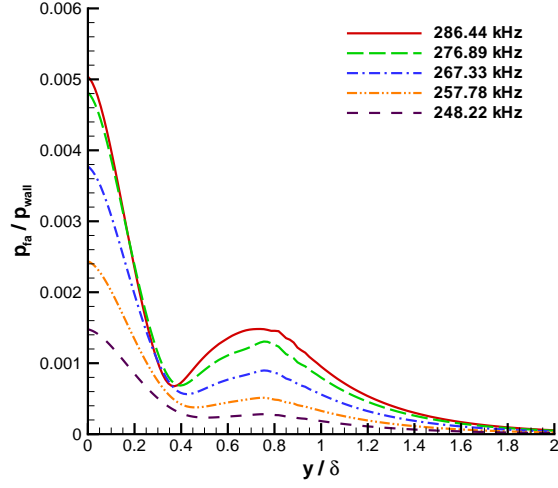
independent of spanwise wavenumber, is shown as a 2D stability diagram in Figure 14d along with the second-mode amplification rates. It is clear from Figure 14d that second-mode disturbances have larger peak amplification rates than first-mode disturbances.

Figure 15 plots the maximum first-mode and second-mode  $N$  factors along with corresponding most unstable frequencies and wave angles. The first and second-mode disturbance frequency estimates, generated from the mean flow solution, are also included as a reference. The first-mode oblique wave  $N$  factors are approximately the same values as the second-mode disturbances up to approximately  $x = 0.3$  m. After this axial location the second-mode disturbances have larger integrated growth rates than the first-mode disturbances. This analysis does not yet explain the cause of transition in the experiment since both first and second-mode disturbances had fairly small instability wave growth.

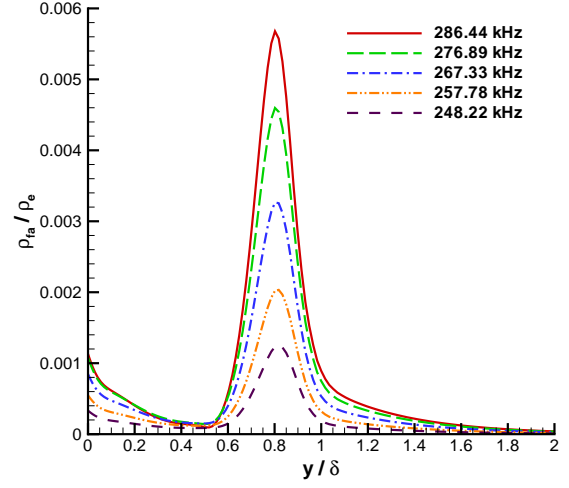
Case	Tunnel	Flow	$Re/m \times 10^6$	$N = 5.5$ (m)	Exp. Lower Bound (m)	Exp. Upper Bound (m)	$N$ range
1	BAM6QT	Noisy	2.9	$> 0.517$	$> 0.490$	$> 0.490$	$> 3.7$
2	BAM6QT	Noisy	6.4	0.373	0.28	0.32	4.5 - 4.9
3	BAM6QT	Noisy	8.5	0.286	0.21	0.25	4.4 - 5.0
4	BAM6QT	Noisy	10.4	0.224	$< 0.208$	0.21	$\leq 5.0$
5	BAM6QT	Quiet	10.3	0.204	$> 0.490$	$> 0.490$	$> 9.9$
6	HWT-5	Noisy	5.7	$> 0.517$	0.45	0.49	3.1 - 3.3
7	HWT-5	Noisy	9.1	$> 0.517$	0.36	0.40	3.6 - 3.7
8	HWT-8	Noisy	5.0	0.482	0.45	0.49	5.3 - 5.6
9	HWT-8	Noisy	9.5	0.230	0.28	0.32	6.3 - 6.7

Table 4. Estimated and observed transition locations from the simulations and experiments.

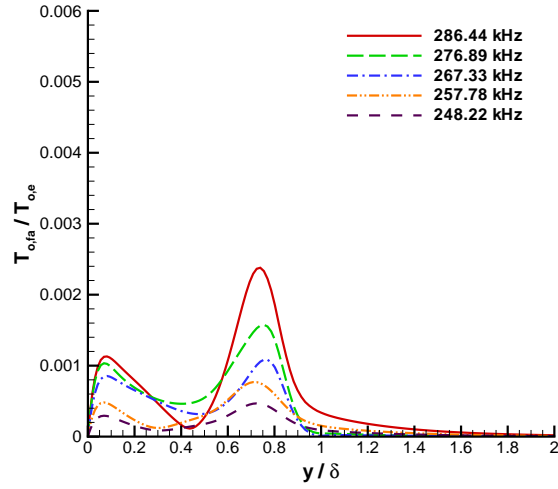




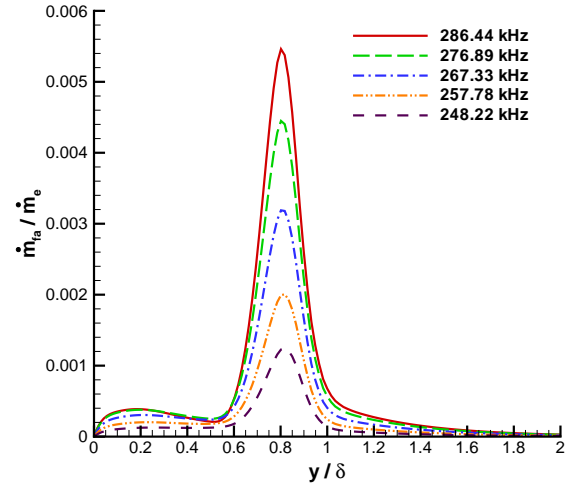
(a) Pressure fluctuation normalized by wall pressure



(b) Density fluctuation normalized by edge density



(c) Total temperature fluctuation normalized by edge total temperature



(d) Mass flux fluctuation normalized by edge mass flux

**Figure 11.** Case 2 normalized disturbance fluctuation amplitude results at a surface pressure sensor location of  $x = 0.208$  m. The amplitudes for each variable are scaled to maximum pressure fluctuations of 1% of freestream pressure at  $x = 0.208$  m. The x-axis is distance from wall, normalized by the boundary-layer thickness  $\delta$  (99.5% of  $h_o$ ).

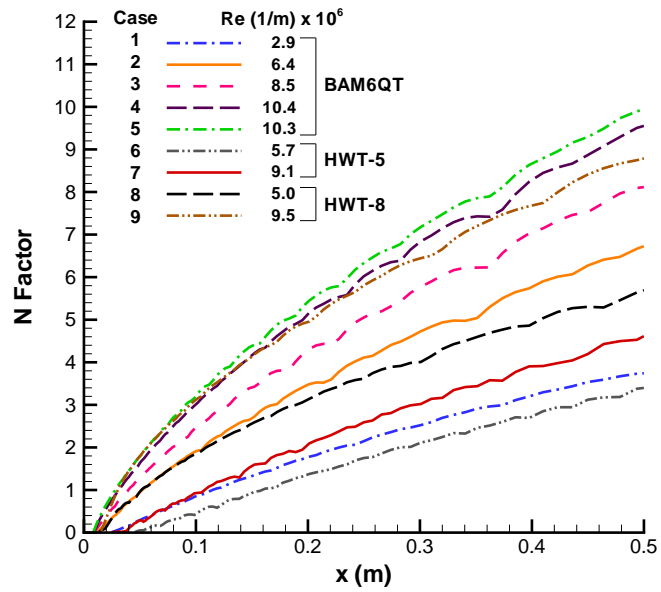


Figure 12. Maximum  $N$  factors for all cases. Note that Cases 1-4 were run noisy and Case 5 was run quiet.

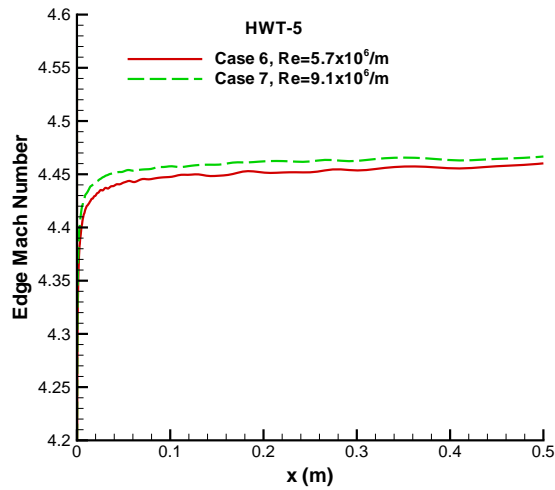
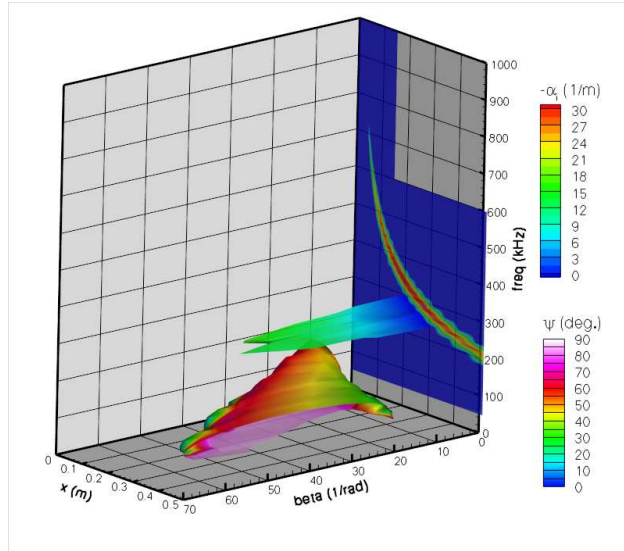
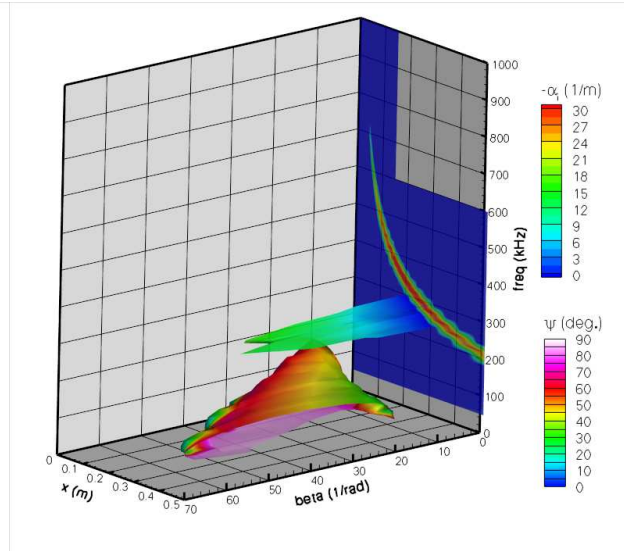


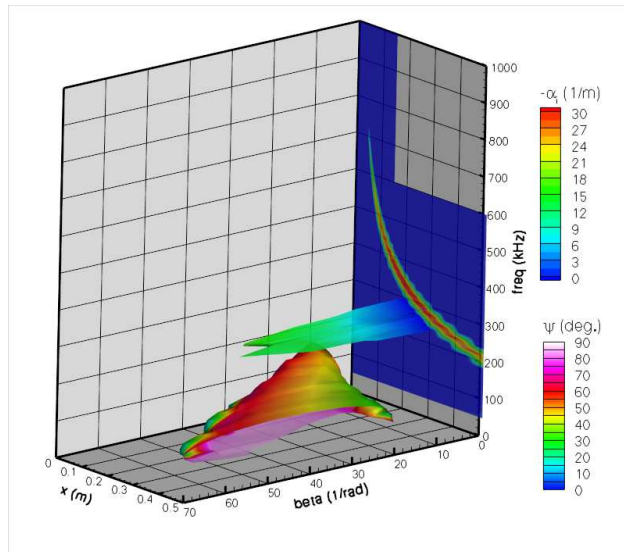
Figure 13. Edge Mach number comparison for Cases 6 and 7.



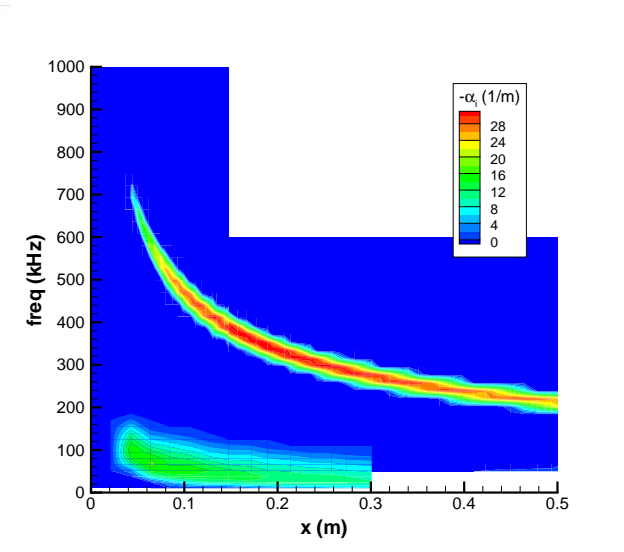
(a) 3D stability diagram, angle 1



(b) 3D stability diagram, angle 2



(c) 3D stability diagram, angle 3



(d) 2D stability diagram

Figure 14. Combined first-mode and second-mode disturbance stability diagrams for Case 6.

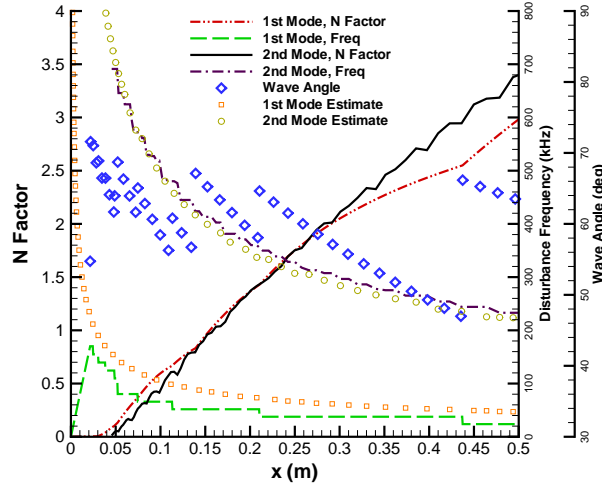


Figure 15. First-mode and second-mode disturbance stability results for Case 6.

## V. Conclusions

Linear stability calculations of second-mode wave instabilities on a  $7^\circ$  half-angle cone at zero angle of attack were compared to experiments carried out in Purdue University's BAM6QT and Sandia National Laboratories HWT-5 and HWT-8. This was the first time that second-mode waves were successfully measured in the Sandia Hypersonic Wind Tunnel. The experiments utilized PCB132 pressure transducers to measure second-mode waves and determine boundary-layer transition onset locations. The agreement between computations and experiments in determining the most amplified second-mode disturbance frequency varied between a 2% and 14% accuracy. The best second-mode frequency comparisons occurred at the highest freestream Mach and Reynolds number tested. It appeared that second-mode waves were not the dominant transition mechanism for the HWT-5 cases and possible nonlinear wave growth effects were present. Attempts at comparing amplitude ratios were made but large errors were seen under the quiet flow condition. The uncertainty associated with the PCB132 amplitude measurements is still unknown. Also, higher harmonics were present in the experiment so we should expect disagreement from calculated linear amplification rates.

The computed disturbance eigenfunctions were also given for one of the cases. Second-mode wave amplitudes were scaled and normalized using mean flow edge or wall conditions. These eigenfunction plots show the aspects of a wave which are more readily measured in experiments. An improved understanding of the spatial variations in the second-mode waves and of the relative amplitudes of the various components of the fluctuations will aid in the design of future instrumentation.

Lastly,  $e^N$  calculations were used to determine a  $N$  factor for transition onset prediction in both tunnels. It was found that a conventionally run BAM6QT had a correlating transition onset  $N$  factor value between 4.5 and 5.0, which is lower than what has been previously published for other conventional wind tunnels. The one quiet case in the BAM6QT did not have an observed transition location and a  $N$  factor of about 10 was reached by the end of the cone. The HWT-8 had a correlating  $N$  factor around 5.5 for the lower unit Reynolds number case and a  $N$  factor of 6.5 for the higher unit Reynolds number case. More tests are needed to build upon the  $N$  factor correlation for this tunnel. The HWT-5 cases had observed transition onset locations in the experiment when the second-mode  $N$  factors were fairly low. A first-mode oblique wave disturbance analysis was performed only to conclude that they did not appear to be a dominant transition mechanism either. Nonlinear wave growth or nonlinear mode interactions could be the cause of transition for these cases.

## VI. Acknowledgments

The authors would like to recognize NDSEG, AFOSR and Sandia National Laboratories for their support of the experimental work. Sandia is a multiprogram laboratory operated by Sandia Corporation, a Lockheed Martin Company, for the United States Department of Energy's National Nuclear Security Administration under contract DE-AC04-94AL85000. The authors would also like to thank to Dr. Heath Johnson and Justin Smith for initial computations for the cone and for several discussions concerning the eigenfunction analysis. Thank you to John Henfling, Rusty Spillers, and Brian Pruett for making the Sandia HWT tests possible. The Purdue Ludwig Tube group also provided help and support for the BAM6QT experiments. Computational resources were made available by the DoD Supercomputing Resource Center at the Air Force Research Laboratory.

## References

- <sup>1</sup>Mack, L. M., "Boundary-Layer Linear Stability Theory," *Special Course on Stability and Transition of Laminar Flow*, AGARD-R-709, chap. 3, June 1984, pp. 3–1:3–81.
- <sup>2</sup>Stetson, K., Kimmel, R., Thompson, E., Donaldson, J., and Siler, L., "A Comparison of Planar and Conical Boundary Layer Stability at a Mach Number of 8," Paper 91-1639, AIAA, June 1991.
- <sup>3</sup>Stetson, K. F. and Kimmel, R. L., "Example of Second-Mode Instability Dominance at a Mach Number of 5.2," *AIAA Journal*, Vol. 30, No. 12, December 1992, pp. 2974–2976.
- <sup>4</sup>Schneider, S. P., "Hypersonic Laminar-Turbulent Transition on Circular Cones and Scramjet Forebodies," *Progress in Aerospace Sciences*, Vol. 40, 2004, pp. 1–50.
- <sup>5</sup>Fujii, K., "Experiment of Two Dimensional Roughness Effect on Hypersonic Boundary-Layer Transition," *Journal of Spacecraft and Rockets*, Vol. 43, No. 4, July-August 2006, pp. 731–738.
- <sup>6</sup>Estorf, M., Radespiel, R., Schneider, S. P., Johnson, H., and Hein, S., "Surface-Pressure Measurements of Second-Mode Instability in Quiet Hypersonic Flow," Paper 2008-1153, AIAA, January 2008.
- <sup>7</sup>Tanno, H., Komuro, T., Sato, K., Itoh, K., Takahashi, M., and Fujii, K., "Measurement of Hypersonic Boundary Layer Transition on Cone Models in the Free-Piston Shock Tunnel Hiest," Paper 2009-0781, AIAA, January 2009.
- <sup>8</sup>Johnson, H. B. and Candler, G. V., "Hypersonic Boundary Layer Stability Analysis Using PSE-Chem," Paper 2005-5023, AIAA, June 2005.
- <sup>9</sup>Casper, K. M., *Hypersonic Wind-Tunnel Measurements of Boundary-Layer Pressure Fluctuations*, Master's thesis, Purdue University School of Aeronautics and Astronautics, August 2009.
- <sup>10</sup>Juliano, T., Schneider, S., Aradrag, S., and Knight, D., "Quiet-Flow Ludwig Tube for Hypersonic Transition Research," *AIAA Journal*, Vol. 46, No. 7, 2008, pp. 1757–1763.
- <sup>11</sup>Schneider, S. P., "The Development of Hypersonic Quiet Tunnels," *Journal of Spacecraft and Rockets*, Vol. 45, No. 4, July-August 2008, pp. 641–664.
- <sup>12</sup>Casper, K. M., Beresh, S. J., Henfling, J. F., Spillers, R. W., Pruett, B., and Schneider, S. P., "Hypersonic Wind-Tunnel Measurements of Boundary-Layer Pressure Fluctuations," Paper 2009-4054, AIAA, June 2009, revised November 2009.
- <sup>13</sup>Wright, M. J., Candler, G. V., and Bose, D., "A Data-Parallel Line-Relaxation Method for the Navier-Stokes Equations," Paper 97-2046CP, AIAA, June 1997.
- <sup>14</sup>Schneider, S. P., "Hypersonic Laminar Instability on Round Cones Near Zero Angle of Attack," Paper 2001-0206, AIAA, January 2001.
- <sup>15</sup>Collicott, S., Schneider, S., and Messersmith, N., "Review of Optical Diagnostics for Hypersonic Low-Noise Ludwig Tube Facilities," Paper 96-0851, AIAA, January 1996.
- <sup>16</sup>Johnson, H. B., Alba, C. R., Candler, G. V., MacLean, M., Wadhams, T., and Holden, M., "Boundary-Layer Stability Analysis of the Hypersonic International Flight Research Transition Experiments," *Journal of Spacecraft and Rockets*, Vol. 45, No. 2, March-April 2008, pp. 228–236.
- <sup>17</sup>Alba, C. R., Johnson, H. B., Bartkiewicz, M. D., Candler, G. V., and Berger, K. T., "Boundary-Layer Stability Calculations for the HIFiRE-1 Transition Experiment," *Journal of Spacecraft and Rockets*, Vol. 45, No. 6, November-December 2008, pp. 1125–1133.
- <sup>18</sup>Jaffe, N. A., Okamura, T. T., and Smith, A. M. O., "Determination of Spatial Amplification Factors and Their Application to Predicting Transition," *AIAA Journal*, Vol. 8, No. 2, February 1970, pp. 301–308.
- <sup>19</sup>Chen, F.-J., Malik, M. R., and Beckwith, I. E., "Boundary-Layer Transition on a Cone and Flat Plate at Mach 3.5," *AIAA Journal*, Vol. 27, June 1989, pp. 687–693.
- <sup>20</sup>Malik, M. R., "Hypersonic Flight Transition Data Analysis Using Parabolized Stability Equations with Chemistry Effects," *Journal of Spacecraft and Rockets*, Vol. 40, No. 3, May-June 2003.
- <sup>21</sup>Johnson, H. B. and Candler, G. V., "Analysis of Laminar-Turbulent Transition in Hypersonic Flight Using PSE-Chem," Paper 2006-3057, AIAA, June 2006.
- <sup>22</sup>Alba, C. R., Johnson, H. B., and Candler, G. V., "Oblique Wave Disturbance Analysis of Supersonic Flow Past Axisymmetric and 2D Bodies at Angles of Attack," Paper 2008-4396, AIAA, June 2008.